

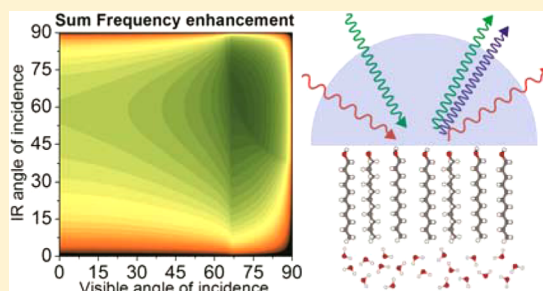
# Vibrational Sum Frequency Spectroscopy Studies at Solid/Liquid Interfaces: Influence of the Experimental Geometry in the Spectral Shape and Enhancement

Jonathan F. D. Liljeblad and Eric Tyrode\*

Surface and Corrosion Science, Department of Chemistry, KTH Royal Institute of Technology, SE-100 44, Stockholm, Sweden

**S** Supporting Information

**ABSTRACT:** The influence of the experimental geometry, specifically the angles of incidence (AOI) of the exciting beams, on the enhancement of the vibrational sum frequency spectroscopy (VSFS) spectra has been systematically investigated, particularly when approaching total internal reflection (TIR) conditions. Theoretical simulations of the spectral intensity as a function of the AOI and infrared wavelength at three different polarization combinations were critically compared to experimental data obtained from a hydrophobized silica/water interface. The spectra were recorded using a newly established femtosecond VSFS spectrometer designed to allow rapid and accurate changes of the angles of incidence. At the most favorable AOI, when the IR, visible, and/or emitted sum frequency beams were close to TIR conditions, the spectral enhancement could be up to several orders of magnitude. The effect from the IR beam was however less pronounced due to absorption from the aqueous phase. Furthermore, the relative enhancement of the spectral features across the CH and OH stretching regions varied significantly depending on the angles of incidence chosen. The uneven enhancement is a consequence of the large dispersion in the IR refractive index of water. Although the theoretical simulations qualitatively predict this trend, the quantitative agreement with the experimental data is poor. The simulations underestimate the amplification in the free OH range by 2–4 times as the IR beam approaches TIR, and overestimates it as the visible beam approaches the critical angle. These observations may suggest a need to review the fundamental equations describing the angular dependence of the SF intensity. The practical advantages of selecting specific angles of incidence, as well as the expected variations for two other frequently encountered solid/liquid interfaces (CaF<sub>2</sub>/water and sapphire/water), are also discussed.



## 1. INTRODUCTION

Since first demonstrated a quarter of a century ago,<sup>1</sup> vibrational sum frequency spectroscopy (VSFS) has proven to be a valuable tool for probing the structure and conformation of molecules present at many fundamentally and technologically relevant interfaces.<sup>2–5</sup> In particular, VSFS has shown an exceptional ability to selectively probe surface molecules at buried interfaces (e.g., solid/liquid and liquid/liquid interfaces), which are among the most complicated to examine with traditional surface science techniques.<sup>6</sup> The sum frequency (SF) signal generated at the interfacial region is usually weak. At buried interfaces, however, it is generally possible to significantly enhance the SF intensity by delivering the incident beams at, or close to, total internal reflection (TIR) conditions.<sup>7,8</sup> This approach has been widely used when targeting, for example, liquid/liquid<sup>9–11</sup> and solid/liquid<sup>12–15</sup> interfaces.

Although the theoretical foundations of the angular dependence of the SF intensity are well established,<sup>8,16–18</sup> only a few studies have systematically compared, albeit to a limited extent, experimental data with theoretical predictions.<sup>8,13</sup> These studies have largely confirmed the expected overall enhancement when the critical angles are approached. Nonetheless, experimental

challenges associated with keeping the spatial and temporal overlaps while changing the angles of incidence during a single experiment<sup>19</sup> have hampered a direct comparison, even in qualitative terms, of a number of frequency- and angular-dependent features predicted by the theory to occur close to TIR conditions. In the present study, we address these limitations measuring the variations in the SF spectra at selected angles of incidence using a recently developed SF spectrometer, specifically designed to allow rapid and precise changes in the angles of incidence.

The model system chosen for these studies is a hydrophobic solid in contact with water. The solid consists of a self-assembled silane monolayer (octadecyltrichlorosilane) chemically attached to a fused silica substrate. The interactions of water with the hydrophobic monolayer give rise to spectral features across a broad frequency region (CH and OH stretching vibrations). This is important for testing the predicted changes in the relative enhancement of the SF intensity between different spectral regions as a function of the

Received: July 10, 2012

Revised: October 5, 2012

Published: October 8, 2012



experimental geometry. Moreover, a hemispherical-shaped silica substrate was selected to avoid any potential angular- and polarization-dependent losses when delivering the laser beams and facilitate the direct comparison of the spectra collected at different angles of incidence and polarization combinations.

Self-assembled hydrophobic monolayers similar to the model system used here have been the subject of increased interest as model systems to explore the molecular structure of water and ion behavior close to hydrophobic surfaces.<sup>20–24</sup> As will be clearly demonstrated in this work, the experimental geometry chosen will simplify or may even have an influence on the interpretation of the recorded data. The conclusion reached, however, extends to other systems including different solid substrates in contact with aqueous solutions, such as  $\text{CaF}_2$  and sapphire.

## 2. EXPERIMENTAL SECTION

**2.1. Materials.** Octadecyltrichlorosilane ( $\geq 96\%$ ) and toluene (anhydrous 99.8%) were purchased from Merck and Sigma-Aldrich, respectively. Both compounds were used as received. The water used in the experiments was obtained from an Integral 15 Millipore filtration unit (resistivity of 18.2  $\text{M}\Omega$  cm and total organic carbon <3 ppb). The IR grade fused silica hemispheres ( $R_a < 0.7$  nm) were custom-made by CVI-Melles Griot. Chromosulphuric acid from Merck was used for cleaning the hemispheres before silanation.

**2.2. Vibrational Sum-Frequency Spectrometer.** The femtosecond VSF spectrometer used for this investigation has been recently established and will be described in detail below. The key elements are, first, a femtosecond pulsed laser source (Ti:Sapphire broadband oscillator and a combined regenerative and multipass amplifier); second, a traveling wave optical parametric amplifier (TOPAS) for generating a tunable infrared pulse; third, a pulse shaper for creating a picosecond 800 nm visible pulse; fourth, motorized polarization control and beam steering optics, and, finally, a combined imaging spectrograph and EM-CCD camera to detect the sum frequency signal.

**2.2.1. Laser.** The laser source consists of a Ti:light-200 oscillator and an Integra-HE-7-FS amplifier (both from Quantronix, U.S.). The self-mode-locked Ti:Sapphire oscillator, which is pumped with a 532 nm, 2.5 W CW frequency doubled Nd:YVO<sub>4</sub> laser (Colibri, Quantronix), generates an 87 MHz pulse train centered at 800 nm, with a bandwidth >30 nm and average power of 300 mW. This pulse is propagated through a bandpass filter to limit the bandwidth to 13 nm before directing it to the amplifier. The Integra-HE chirped pulse amplifier features two Ti:Sapphire crystals: the first is utilized in a regenerative amplifier (RGA) and the second in a dual pass (multipass) amplifier. The amplifiers are pumped with two 527 nm, Q-switched Nd:YLF lasers with intracavity LBO frequency doubling (Darwin, Quantronix). Typically, the Integra delivers a 1 kHz train of pulses with a total power of 6.2 W. Each pulse is approximately 90 fs long and is centered at 806 nm with a bandwidth of  $\sim 10$  nm.

**2.2.2. TOPAS.** A traveling optical wave parametric amplifier HE-TOPAS-C, with noncollinear DFG mixing stage (Light Conversion, Lithuania), is used to generate the infrared pulse. The TOPAS, tunable between 1.14 and 20  $\mu\text{m}$  (8770–500  $\text{cm}^{-1}$ ), is pumped with 75% of the total output power from the Integra amplifier. The output energies in the CH and OH stretching regions are approximately 100 mW with a bandwidth of 250  $\text{cm}^{-1}$ . Note that, as mentioned below, only a small

fraction of the power generated by the TOPAS is finally directed to the sample.

**2.2.3. Pulse Shaper.** The bandwidth-tunable picosecond pulse is produced in a home-built, folded, 4f pulse shaper. The main elements are a gold-coated grating (1480 grooves/mm, blazed for 800 nm, from Horiba-Jobin Yvon, France), a spherical UV-silica lens (+500 mm focal length), a plane dielectric mirror located in the Fourier plane, and an adjustable micrometer precision slit placed immediately in front of this mirror. Closing the slit decreases the bandwidth and the output energy. The beam shaper is slightly misaligned in the vertical direction to facilitate the separation of the outgoing beam from the incoming beam. Careful alignment was performed to achieve a collimated picosecond beam with minimum chirp.<sup>25</sup> Spectral data are typically recorded with the slit opened between 150 and 500  $\mu\text{m}$ , which is equivalent to an overall resolution of  $<1\text{--}4$   $\text{cm}^{-1}$  in the SF spectra. The output energy of the picosecond beam leaving the pulse shaper is typically 4–14 mW.

**2.2.4. Beam Steering, Polarization Control, and Sample Positioning.** To facilitate the data acquisition, the spectrometer features a high degree of automation, including motorized control of the beam polarizations, the angle of incidence of the visible 800 nm and SF beams, and the IR-power.

The tunable IR beam from the TOPAS is first directed to a manually adjustable delay stage to ensure temporal overlap with the 800 nm beam. The polarization of the beam is then turned 45° using reflection optics and led toward two BaF<sub>2</sub> wire grid polarizers placed in motorized rotation stages. The first is used to modulate the power, and the second to select the desired polarization. The power at the sample position is set following an automated procedure, involving the two grid polarizers and a XLP12 detector from Gentec-EO (Canada). The angle of incidence (AOI) of the IR beam is manually set moving an integrated linear and rotational stage (Newport, U.S.) connected to the last steering mirror before the sample position. With this configuration, the IR AOI can be set with a precision better than 0.02° in just a matter of minutes. The IR beam is finally focused immediately after the sample position using a BaF<sub>2</sub> lens (+200 mm focal length) mounted on a precision translation stage. To avoid IR losses due to water vapor absorption bands, the IR beam path is purged by an overpressure of dry air.

On the visible arm, the polarization of the narrow-band beam is selected by a tunable  $\lambda/2$  plate followed by a MgF<sub>2</sub> Rochon polarizer (both from Alphalas, Germany). The beam is sent through a motorized delay stage (Newport, U.S.) that is adjusted to maintain the temporal overlap at the sample when the visible AOI is varied. The visible beam is gently focused just behind the sample position using a +1000 mm silica lens. The setting of the visible AOI as well as the collection angle in the sum frequency (SF) arm are fully motorized. Gimbal mounts holding the directing mirrors are attached to integrated motorized rotational and linear translational stages (Newport, USA) to control the angle and vertical positions. The AOI in the motorized stages can be set in seconds with a precision better than 0.01°.

A careful alignment of the sample and laser beams is crucial when using a hemispherical geometry. For such purpose, a modified white light microscope (Infinity Photo-Optical, U.S.) with a long working distance objective (Mitutoyo, Japan) is mounted above the sample position. This allows setting the hemisphere position with micrometer precision and high

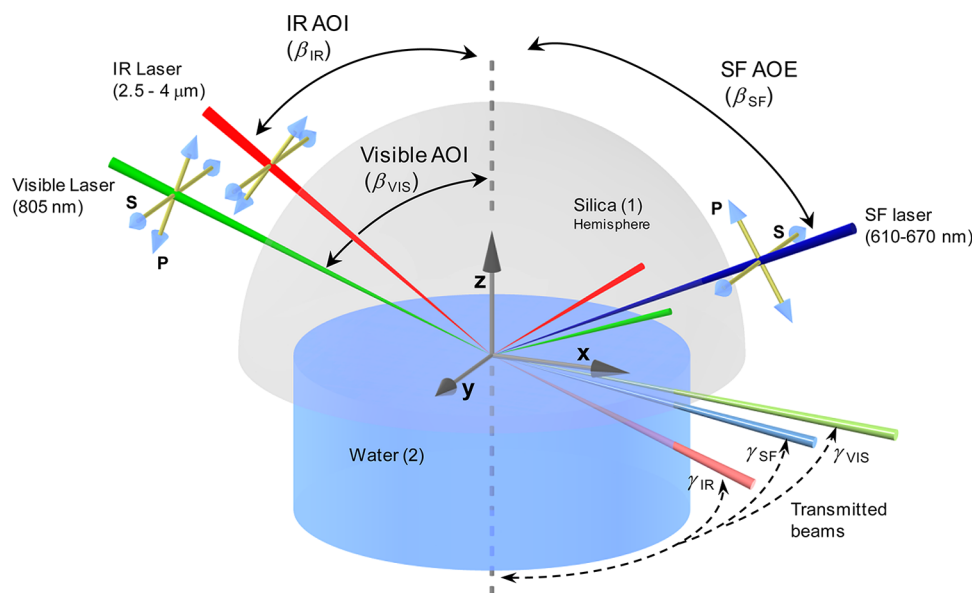


**Figure 1.** Diagram of the experimental cell showing the laser beams at the sample position. All laser beams propagate in the  $xz$  plane in a copropagating geometry. In P-polarized light, the electric field oscillates parallel to the plane of incidence ( $xz$  plane), while in S-polarization it oscillates perpendicular to the  $xz$  plane. AOI and AOE stand for angle of incidence and angle of emission, respectively.

reproducibility. The typical energies and beam diameters at the sample position are 4 mW and 150  $\mu\text{m}$ , and 10 mW and 350  $\mu\text{m}$ , for the IR and visible beams, respectively.

**2.2.5. Detection and Acquisition.** The motorized SF arm is programmed to change position depending on the angle of emission of the SF beam. The SF light is then collimated and directed to a tunable  $\lambda/2$  plate and a  $\text{MgF}_2$  Rochon polarizer (both from Alphalas, Germany). The combination of the last two optical elements allows selecting the desired SF polarization and ensures that the polarization of the beam reaching the spectrometer is always horizontal. This is important for avoiding polarization-dependent losses and maximizing the spectrometer efficiency. Before reaching the spectrometer (Shamrock SR-303i-B, Andor, Ireland), the SF beam is first spatially and optically filtered, using a slit placed between two positive lenses, and a short-pass filter (RazorEdge 785 nm, Semrock, U.S.), respectively. This prevents any 800 nm stray light from reaching the detector. The SF beam is finally focused on the spectrometer entrance slit. The detector consists of an EM-CCD camera (Newton DU971N-UVB, Andor, Ireland) directly attached to the exit port of the spectrometer. On the basis of the grating used and the number and size of pixels in the CCD chip, the highest possible resolution attainable is 0.8  $\text{cm}^{-1}$ . The actual resolution of the spectrometer, however, depends on other parameters such as the spectrometer slit size and the visible beam bandwidth. Experimentally, the maximum attainable resolution of the spectrometer is better than 1  $\text{cm}^{-1}$ . This is assessed by comparing the nonresonant SF spectra of gold in humid air at different visible beam bandwidths (Figure S1 in the Supporting Information). A slightly better resolution ( $\sim 0.6 \text{ cm}^{-1}$ ) could in principle be obtained following the approach proposed by Wang and co-workers;<sup>26</sup> nonetheless, such resolution is generally not required as the intrinsic vibrational line widths in liquids are usually  $>2 \text{ cm}^{-1}$ .<sup>27</sup>

**2.3. Data Normalization and Assembling of Final Spectrum.** Spectral peaks in the recorded data are convolved with the Gaussian shape of the IR intensity. To restore the true peak intensities and shapes, a normalization procedure is

required. In this Article, the nonresonant SF signal from gold is used as reference. The gold layer (100 nm thick) is deposited on a silica hemisphere identical to those used for the silane monolayers. The use of gold as reference implies assuming that its SF response is frequently independent in the spectral range considered (i.e., truly nonresonant). The normalization procedure consists of dividing the sample spectra by the corresponding gold spectra collected at the same IR center frequencies and IR and visible AOIs. This normalization procedure also allows accounting for a number of potentially angular dependent factors, including variations in the power density at the sample position, which decreases with increasing angles of incidence. This is necessary for making a quantitative comparison possible. Additionally, to avoid amplifying noise from the low intensity wings, the raw data are truncated at approximately 10% of the maximum signal intensity in the reference spectra. The normalized spectra at different IR center frequencies are then added together to obtain the final spectrum. The procedure outlined above, including the raw and normalized spectra, is described in more detail in the Supporting Information (Figure S2).

**2.4. Sample Preparation and Handling.** The measuring cell consisted of an IR grade fused silica hemisphere (5 mm in radius) sealed with a Viton O-ring to the top of a custom-made glass cell. The two incoming laser beams were carefully overlapped at the center of the hemisphere as verified with a white light microscope. The hemispherical geometry assures that the different laser beams experience the same Fresnel losses at the curved surface, regardless of the angles of incidence and polarizations chosen. Degassed water was injected through a glass capillary positioned a few millimeters below the center of the hemisphere. Before silanization, the silica hemisphere was cleaned using chromosulphuric acid, where it was first soaked for at least 2 h, rinsed copiously in ultrahigh purity water, sonicated, and finally rinsed once again in water. All other items including glassware, Teflon valves, tubing, and Viton O-rings were cleaned with a commercial alkaline agent (Deconex 11 Universal from Borer Chemie) and



rinsed thoroughly with water. The OTS monolayer was assembled by immersing the hemisphere in a  $\sim 2$  mM solution of OTS in toluene for  $\sim 12$  h. This procedure was carried out in a water vapor-free atmosphere. The hemisphere was then rinsed several times and sonicated in toluene, later rinsed three times in ethanol, and subsequently placed in an oven at  $110^\circ\text{C}$  for 1 h. The acquisition time for each SF spectra was 10–20 min (1–2 min per IR frequency step). All spectra were collected at  $21^\circ\text{C}$ . The experiments shown here were repeated on at least three different occasions. The same silane monolayer was used when collecting all of the spectra presented in this work.

### 3. THEORETICAL PRINCIPLES OF VSFS

VSFS is a second order nonlinear optical technique with an inherent surface specificity and submonolayer sensitivity. It can be applied to any interface accessible to the laser beams and enables the determination of the orientation of molecular species. In practical terms, two pulsed laser beams, one tunable in the IR region and the other fixed in the visible region, are overlapped in time and space at an interface, and the intensity of a third beam generated at the interface at the sum of the frequencies of the two incoming beams is measured as a function of the IR wavelength. Being an established technique, its theoretical foundations are well described in the literature,<sup>2,28–30</sup> and only a summary of the most relevant principles, in particular those responsible for the angular dependence of the sum frequency response, will be given here.

The spatial direction of the emitted SF beam is dictated by the conservation of momentum in the  $x$  direction (Figure 1). For a copropagating geometry, the intensity of the SF beam is described by eq 1, where  $I_i$  refers to the intensities of the incident fields,  $\chi_{\text{eff}}^{(2)}$  to the effective susceptibility tensor, and  $n_i(\omega_i)$  to the refractive indexes of the incident media (Figure 1).

$$I_{\text{SF}}(\omega_{\text{SF}}) = \frac{8\pi^3 \omega^2 \sec^2 \beta_{\text{SF}}}{c^3 n_1(\omega_{\text{SF}}) n_1(\omega_{\text{VIS}}) n_1(\omega_{\text{IR}})} |\chi_{\text{eff}}^{(2)}|^2 I_1(\omega_{\text{VIS}}) I_2(\omega_{\text{IR}}) \quad (1)$$

The two tensors  $\chi_{\text{eff}}^{(2)}$  and  $\chi^{(2)}$  are related by the unit polarization vectors,  $\hat{\mathbf{e}}$ , and the tensor  $L'(\omega)$  (eq 2). This latter tensor is the product of  $L(\omega)$ , the macroscopic Fresnel factors, and  $l(\omega)$ , the microscopic local field factors.

$$\chi_{ijk,\text{eff}}^{(2)} = [\mathbf{e}_i L'_{ii}(\omega_{\text{SF}})] \cdot \chi_{ijk}^{(2)} : [\mathbf{L}'_{jj}(\omega_{\text{VIS}}) \mathbf{e}_j] [\mathbf{L}'_{kk}(\omega_{\text{IR}}) \mathbf{e}_k] \quad (2)$$

For a copropagating geometry, the unit vectors for S- or P-polarized beams are:

$$\begin{aligned} e_x &= \cos \beta \\ e_y &= 1 \\ e_z &= \pm \sin \beta \end{aligned} \quad (3)$$

The macroscopic Fresnel factors  $L_{nn}$  are:<sup>31,32</sup>

$$L_{XX}(\Omega) = \frac{2n_1(\Omega) \cos \gamma}{n_1(\Omega) \cos \gamma + n_2(\Omega) \cos \beta} \quad (4)$$

$$L_{YY}(\Omega) = \frac{2n_1(\Omega) \cos \beta}{n_1(\Omega) \cos \beta + n_2(\Omega) \cos \gamma} \quad (5)$$

$$L_{ZZ}(\Omega) = \frac{2n_2(\Omega) \cos \beta}{n_1(\Omega) \cos \gamma + n_2(\Omega) \cos \beta} \quad (6)$$

Properly accounting for the microscopic local field factors is far from trivial, and it still remains a subject of debate. To date, analytical expressions have only been derived for a few special cases.<sup>31,33</sup> The most common approach followed in the SF literature is based on a macroscopic three-layer model originally proposed by Shen and Heinz,<sup>16,17</sup> which consists of an infinitely thin polarization sheet sandwiched between two bulk media. The thin sheet was assigned a “refractive index”,  $n'$ , which was later interpreted as the ratio of the microscopic local field factors,  $l_{xx} = l_{yy}$  over  $l_{zz}$ .<sup>18</sup> This model results in a modified expression for  $L_{zz}$  where eq 6 is multiplied by the factor  $((n_1/(n'))^2)$ . It is worth noting that different Fresnel expressions based on the same three-layer model are found in the literature.<sup>30,34,35</sup> These expressions do not necessarily agree with each other (see the Supporting Information for an overview).

Recently, a different approach based on microscopic molecular optics has been proposed for deriving the microscopic local field factors.<sup>31</sup> From this method, the local field factors can in principle be estimated from molecular polarizabilities, after defining a microscopic point-dipole model for the interfacial layer. Although this approach potentially offers a deeper molecular insight, the number of parameters and assumptions required (e.g., the functional group's tilt angle, distribution, surface density, anisotropic molecular polarizabilities, and their frequency dependence) significantly limit its practical use (many of the required parameters are actually the very purpose of the SF measurements in the first place). In this work, Shen's formulation in terms of an  $n'$  will be adopted. Nonetheless, regardless of the approach followed, we note that the local field factors, in contrast to the Fresnel factors, are independent of the angles of incidence and emission of the different laser beams involved in the SF process.

To proceed, expanding eq 2 for the  $\chi^{(2)}$  tensor elements that are nonzero in isotropic interfaces gives:

$$\chi_{\text{eff,SSP}}^{(2)} = L'_{YY}(w_{\text{SF}}) L'_{YY}(w_{\text{VIS}}) L'_{ZZ}(w_{\text{IR}}) \sin \beta_{\text{IR}} \chi_{yyz}^{(2)} \quad (7)$$

$$\chi_{\text{eff,SPS}}^{(2)} = L'_{YY}(w_{\text{SF}}) L'_{ZZ}(w_{\text{VIS}}) L'_{YY}(w_{\text{IR}}) \sin \beta_{\text{VIS}} \chi_{yzy}^{(2)} \quad (8)$$

$$\begin{aligned} \chi_{\text{eff,PPP}}^{(2)} &= -L'_{XX}(w_{\text{SF}}) L'_{XX}(w_{\text{VIS}}) L'_{ZZ}(w_{\text{IR}}) \cos \beta_{\text{SF}} \cos \beta_{\text{VIS}} \sin \beta_{\text{IR}} \chi_{xxx}^{(2)} \\ &\quad - L'_{XX}(w_{\text{SF}}) L'_{ZZ}(w_{\text{VIS}}) L'_{XX}(w_{\text{IR}}) \cos \beta_{\text{SF}} \sin \beta_{\text{VIS}} \cos \beta_{\text{IR}} \chi_{xzz}^{(2)} \\ &\quad + L'_{ZZ}(w_{\text{SF}}) L'_{XX}(w_{\text{VIS}}) L'_{XX}(w_{\text{IR}}) \sin \beta_{\text{SF}} \cos \beta_{\text{VIS}} \cos \beta_{\text{IR}} \chi_{zxx}^{(2)} \\ &\quad + L'_{ZZ}(w_{\text{SF}}) L'_{ZZ}(w_{\text{VIS}}) L'_{ZZ}(w_{\text{IR}}) \sin \beta_{\text{SF}} \sin \beta_{\text{VIS}} \sin \beta_{\text{IR}} \chi_{zzz}^{(2)} \end{aligned} \quad (9)$$

where the SSP and SPS polarization combinations probe single tensor elements, whereas PPP probes an admixture of four elements.

If the refractive index  $n_1$  exceeds  $n_2$ , total internal reflection (TIR) occurs at angles of incidence above the critical angle,  $\Theta_c$ . Note that at  $\Theta_c$  the values of  $L_{yy}$  and  $L_{zz}$  reach a maximum, while  $L_{xx}$  equals zero (see eqs 4–6). This has significant implications for how variations of the experimental geometry influence the resulting spectrum, in particular in the PPP polarization combination.<sup>8</sup> Moreover, when the angle of incidence exceeds  $\Theta_c$ , the Fresnel factors become complex quantities where the imaginary part describes the phase shift of the reflected beam.<sup>7</sup> In addition, the complex refractive indexes must be used to account for the absorption because it has a

prominent influence on the amplification of the fields at TIR conditions.<sup>7</sup> This is particularly relevant for the IR laser beam.

The susceptibility tensor usually includes both a resonant and a nonresonant contribution. For dielectric surfaces like the system considered here, the nonresonant part of the susceptibility is negligible. On the other hand, the resonant part is proportional to the number density, as well as the orientationally averaged microscopic second-order hyperpolarizabilities of the individual molecules at the interface. These latter terms are, however, not dependent on the angles of incident chosen and as such not relevant for the discussion that follows.

## 4. RESULTS AND DISCUSSION

### 4.1. Sum Frequency Signal Enhancement as the TIR Conditions are Approached. Theoretical Simulation of the Influence of the IR and Visible Angles of Incidence.

Figure 2 shows a simulation of the sum frequency intensity for

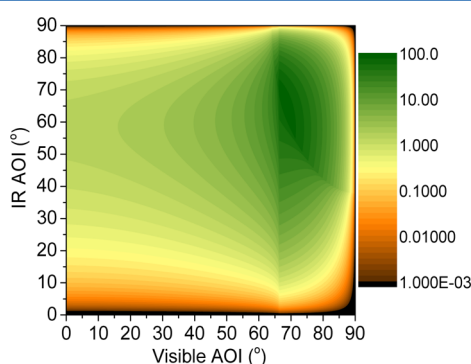


**Figure 2.** Simulation showing the expected variations of the SF intensity for the SSP polarization combination as a function of the IR and visible angles of incidence at a fixed IR wavenumber ( $3350\text{ cm}^{-1}$ ). The data are normalized to 100 for the point with maximum intensity. The vertical and curved ridges correspond to the visible and SF TIR angles, respectively (see text for details).

the SSP polarization combination as a function of the IR and visible angles of incidence at a constant IR wavenumber ( $3350\text{ cm}^{-1}$ ). The SF intensity is determined using eq 7 inserted in eq

1, neglecting the parts that lack angular and frequency dependence, and assuming  $\chi_{ijk}^{(2)}$  to be unity (the actual value of  $n'$  is only relevant for PPP simulations or when taking ratios between different polarization combinations). Complex refractive indexes of water were used for the IR range but not for the visible and SF ranges where the imaginary parts are negligibly small.<sup>36,37</sup> The refractive index of the IR-grade silica hemisphere was modeled using the Selmeier equations<sup>38</sup> (tabulated values for the frequency-dependent refractive index of water and silica used can be found in the Supporting Information). To simplify the interpretation, the simulated data have been normalized setting the highest value to 100. As the angle of incidence or emission approaches the respective  $\Theta_c$  where TIR occurs, the intensity of the signal increases and reaches a maximum close to the intersection of the critical angles of the visible and the SF beams, which is  $\sim 66^\circ$  for both cases. In Figure 2, the visible  $\Theta_c$  appears as a vertical ridge, while the SF  $\Theta_c$ , dependent on both the IR and the visible AOI, is seen as a curved ridge extending from  $65^\circ$  visible AOI and  $90^\circ$  IR AOI to  $90^\circ$  visible AOI and  $35^\circ$  IR AOI. In contrast to the visible and SF beams, the enhancement observed close to the  $\Theta_c$  for the IR beam, which at  $3350\text{ cm}^{-1}$  is approximately  $69^\circ$  as calculated from the real part of the complex refractive index, does not result in an observable enhancement ridge or discontinuity in the rate of change of the SF signal. This is due to the influence of the imaginary (absorption) part of the refractive index that reduces the enhancement near the TIR conditions, replacing the gradient discontinuity with a continuous function.<sup>7,13</sup> The effect of the imaginary part is graphically illustrated in the Supporting Information (Figure S3) where Figure 2 is replotted constraining the water IR refractive indexes to real numbers (in such case, all three ridges at their respective  $\Theta_c$  can be observed).

From Figure 2, it is evident that a substantial enhancement of 4–5 orders of magnitude is expected to occur when approaching the TIR angles from less favorable angles of incidence. Thus, the use of the TIR geometry for collecting spectra in the SSP polarization combination facilitates the detection of weak signals that would otherwise remain indiscernible. Nonetheless, as the refractive index of water varies significantly across the CH and OH stretching regions (e.g., the real part of the refractive index is only 1.12 at  $3540$

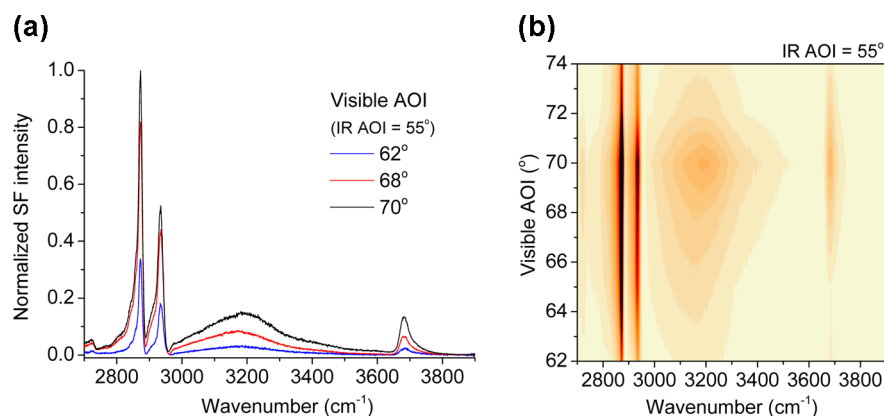


**Figure 3.** Experimental data from the OTS monolayer recorded in the SSP polarization combination at an IR AOI of  $55^\circ$  and various visible angles of incidence. Part (a) shows the increase of the SF signal intensity for three selected visible AOI. The contour plot (b) is based on the experimental data for seven different visible AOI. The contour colors change in the sequence cream  $\rightarrow$  orange  $\rightarrow$  black with increasing SF intensity. The enhancement and subsequent decrease of the SF signal intensity as the visible AOI is increased generally follow the predictions from the simulation shown in Figure 2.

$\text{cm}^{-1}$  and peaks with 1.47 at  $3180 \text{ cm}^{-1}$ ), the best combination of angles will strongly depend on the IR wavenumber (Figure S4 in the Supporting Information shows for comparison the simulated intensity graphs for two additional IR frequencies:  $2880$  and  $3680 \text{ cm}^{-1}$ ). This frequency-dependent enhancement will have important implications in the SF spectra as shown below.

**4.2. Sum Frequency Experimental Data. Influence of the Visible AOI.** The SSP spectra in Figure 3 show the CH and OH stretching regions of the hydrophobic silica/water interface recorded at an IR AOI of  $55^\circ$  and different visible angles. The two prominent bands in the CH region are associated with the terminal methyl group of the silane monolayer, specifically the  $\text{CH}_3$  symmetric stretch ( $r^+$ ) at  $2870 \text{ cm}^{-1}$  and its Fermi resonance ( $r^+_{\text{FR}}$ ) at  $2935 \text{ cm}^{-1}$ . The antisymmetric  $\text{CH}_3$  stretch ( $r^-$ ) at  $2955 \text{ cm}^{-1}$ , which is the strongest band in the PPP and SPS spectra (vide infra), is only observed as a small dip in the SSP spectra due to interference with water bands. Modes associated with the methylene groups (e.g., symmetric  $\text{CH}_2$  stretch at  $\sim 2845 \text{ cm}^{-1}$ ) are practically absent in the spectra, which indicates that the monolayer is tightly packed with a small population of gauche defects.<sup>1,4,39</sup> The OH-stretching region displays two major features, a broad band centered at  $\sim 3200 \text{ cm}^{-1}$  and a sharp band at  $3682 \text{ cm}^{-1}$ . The latter band originates from those few water molecules in direct contact with the silane monolayer having a non-hydrogen-bonded OH group oriented toward the hydrophobic surface.<sup>22,23,40</sup> The former broader band is linked to hydrogen-bonded water molecules forming relatively strong hydrogen bonds. As will be discussed in detail in a forthcoming publication, this broad band is mostly a consequence of interaction of water molecules with the underlying silica surface.

The general trends of the experimental data presented in Figure 3a and b agree with the theoretical predictions (Figure 2). From  $62^\circ$  to  $70^\circ$  visible AOI, the intensity increases almost an order of magnitude and then decreases at angles exceeding  $70^\circ$  as the SF  $\Theta_c$  is passed. The simulation shown in Figure 2 also predicts that the most favorable visible AOI will depend on the IR AOI chosen. For instance, at an IR AOI of  $45^\circ$ , the maximum enhancement is expected at slightly higher visible AOI, while no major changes will be expected at an IR AOI of  $60^\circ$ . This general trend is experimentally confirmed as shown in Figure 4.

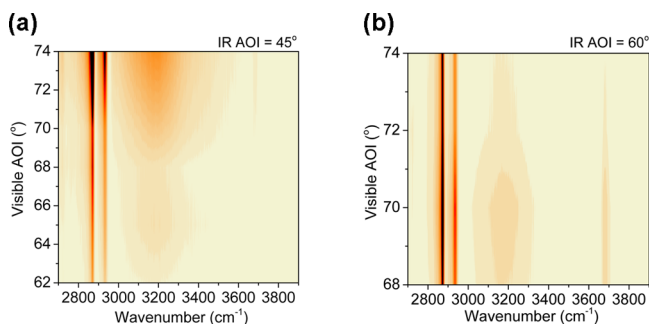


**Figure 4.** Experimental data from the OTS monolayer recorded in the SSP polarization combination at IR AOI of  $45^\circ$  and  $60^\circ$  and various visible angles of incidence. The contour colors and range are similar to those of Figure 3b. The visible angle where the maximum signal intensity is obtained depends on the IR angle chosen, closely following the trends predicted by the theoretical simulations (Figure 2).

**4.3. Unequal Enhancement of Spectral Features across the CH and OH Stretching Regions.** *a. Varying the IR AOI at a Constant Visible AOI.* As shown above, the SF intensity can be enhanced orders of magnitude when selecting the most appropriate angles of incidence. The enhancement, however, is not equal across the CH and OH stretching regions (i.e., the most favorable angles for a CH mode differ from those of an OH mode), making the relative spectral shapes dependent on the angles of incidence chosen. This is particularly evident in the spectra shown in Figure 5, recorded

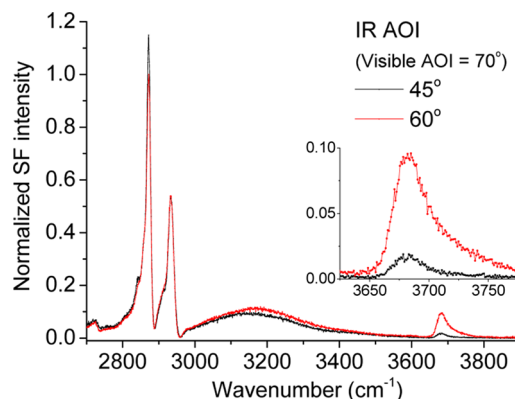


**Figure 5.** Experimental data showing the relative enhancement of the free OH stretching mode for two different IR angles of incidence ( $45^\circ$  and  $60^\circ$ ) at a constant visible angle of incidence ( $70^\circ$ ). Data were recorded in the SSP polarization combination and normalized to the Fermi resonance ( $r^+_{\text{FR}}$ ) at  $2935 \text{ cm}^{-1}$ . The fact that the spectra do not overlap indicates an unequal enhancement across the spectral region.

at two different IR AOI (fixed visible AOI) and normalized to the  $r^+_{\text{FR}}$  peak. The spectra clearly show that the free OH signal is enhanced at  $60^\circ$  as compared to  $45^\circ$  IR AOI. Had the enhancement been equal, the two spectra would have overlapped. The underlying reason for this unequal enhancement is the large variation in the complex refractive index of water across the CH and OH stretching regions (see Table S1 in the Supporting Information). Qualitatively, this general trend is theoretically predicted as shown in the contour plot of Figure 6a. The free OH region is preferentially enhanced at around  $55\text{--}60^\circ$  IR AOI, while the CH region is in turn maximized at an IR AOI of  $75\text{--}80^\circ$ . The quantitative agreement is nevertheless poor. The experimentally observed enhancement is at least 2 times higher than what the simulations predict (Figure 6b).

There are a number of theoretical and experimental factors that could explain this apparent disagreement. From the theoretical perspective, these include any potential inaccuracies in the input parameters used in the simulations, up to deficiencies in the model itself. Considering the former possibility, the only input parameters that influence the magnitude of the enhancement as the IR angle of incidence is varied, while all other parameters are kept constant, are the refractive indexes of silica and water (see eqs 1–7). In particular, we note that whether the macroscopic three-layer model or the microscopic molecular optics approach is used, the refractive index of the thin film ( $n'$ ) as well as the explicit microscopic local field factors are angular independent constants that do not influence the ratios of the prefactors calculated at a given wavenumber. Nevertheless, the refractive indexes of water and silica in the IR frequency range are well-

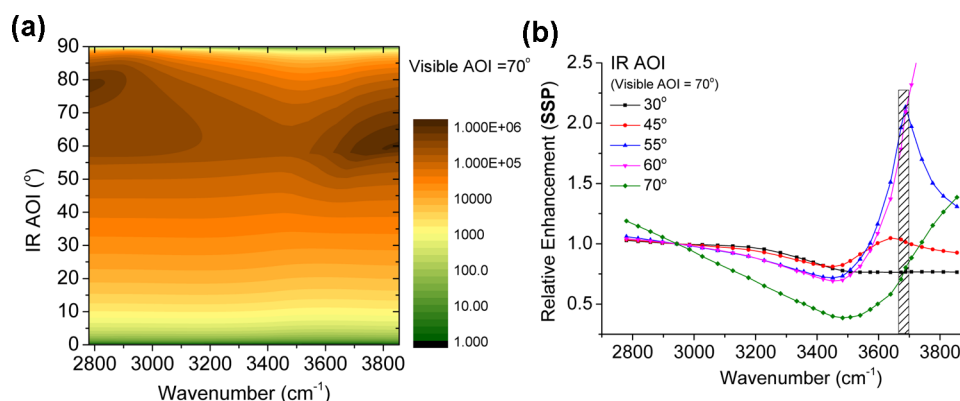


**Figure 6.** Curves calculated for the SSP polarization combination across the CH and OH stretching regions. (a) Simulations showing the expected SF intensity for different IR AOI at a constant visible AOI ( $70^\circ$ ). Note the enhancement of the free OH region at around  $55^\circ$ – $60^\circ$  and that of the CH region at around  $75^\circ$ – $80^\circ$ . (b) Expected relative enhancement across the CH and OH stretching regions for different IR angles of incidence. Data normalized to the intensity at  $2935\text{ cm}^{-1}$ .

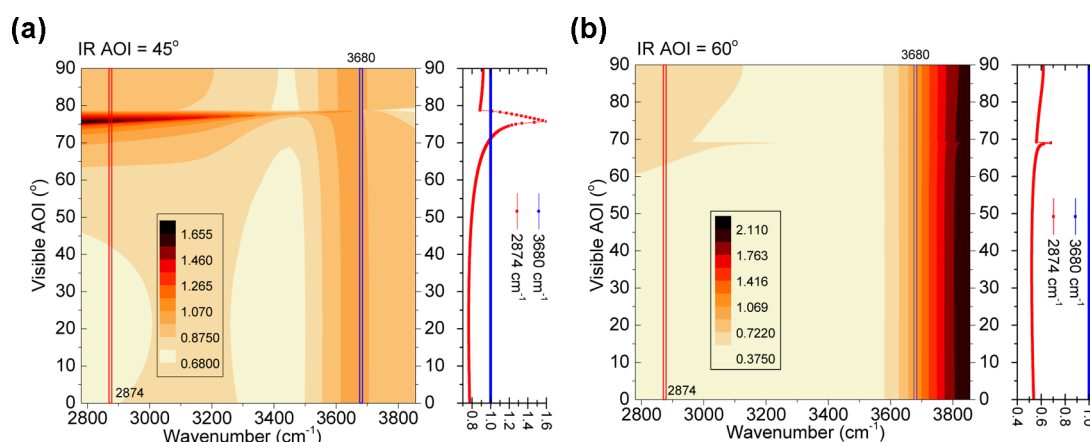


**Figure 7.** Simulations showing the relative enhancement across the CH and OH stretching regions for different visible AOI at two fixed IR AOI ( $45^\circ$  and  $60^\circ$ , respectively). For ease of comparison, the SF intensity was normalized to one at the free OH position ( $3680\text{ cm}^{-1}$ ). The graphs on the right of each figure are relative intensity profiles across two selected frequencies,  $2874$  and  $3680\text{ cm}^{-1}$ , corresponding to the methyl  $r^+$  mode and the free OH vibration of water, respectively. They show how the  $r^+$  mode intensity is expected to vary relative to the free OH band, as a function of the visible AOI.

known, and not even large errors could explain the enhancement observed. For example, the imaginary part of the refractive index of water was found to have the most profound influence, but even if it is set to zero (which is unphysical), it could only account for one-half of the observed difference.

Experimental errors are also unlikely to explain the disagreement between the theoretical predictions and the experimental findings. First, the same silanized hemispherical substrate was used to collected all of the SF spectra presented here, and thus effects associated with the monolayer preparation as described in detail in a forthcoming publication can be disregarded. Second, the powers of the incident lasers were accurately measured and did not vary more than  $\pm 2\%$  within the course of the measurement. Third, the spectra could be repeated with a high degree of reproducibility. Fourth, the normalization procedure based on the nonresonant SF signal from gold allows accounting for a number of potentially angular-dependent factors, which include overlap mismatches of the laser projections at the sample position, as well as the influence of path length differences in the SF collection arm. When normalizing with gold, however, it is implicitly assumed that the Fresnel factors for the gold interface are frequency independent. The complex refractive indexes of gold show only

minor changes in the IR frequency region considered,<sup>41–43</sup> proving that the frequency dependence is indeed negligible.

One factor that differentiates theory from experiments is the spread in the angle of incidence. Although experimentally the laser beams can in principle be set with a precision better than  $0.02^\circ$ , the fact that the beams are converging at the sample position results in an angular spread rather than a single angle of incidence. For the visible beam the spread is  $\pm 0.3^\circ$ , while it is slightly larger for the tighter focused IR beam ( $\pm 0.9^\circ$ ). This implies that a spectrum collected at, for example,  $55^\circ$  IR AOI corresponds in reality to a range of angles comprised between  $54^\circ$  and  $56^\circ$ . Nevertheless, the consequence of this spread of angles in the theoretical predictions is to reduce, in direct opposition to the observed effect, the relative enhancement in the free OH stretching region.

None of the arguments put forward above can realistically explain the observed enhancement. One remaining possibility is that the theoretical model used is not complete. To make the simulated intensity ratios converge with those experimentally measured, an angular-dependent term would need to be included. In the framework of the current models, however, it is difficult to conceive such possibility unless the models themselves are fundamentally flawed.



*b. Varying the Visible AOI at a Constant IR AOI.* The previous discussion has been mainly concerned with the influence of varying the IR angle at a constant visible angle of incidence. The theoretical simulations nonetheless also predict that at a constant IR AOI the enhancement of the CH relative to the free OH region is expected to change when varying the visible AOI, albeit to a much lower extent. The change is expected to be more pronounced when the SF and visible critical angles are the furthest apart (i.e., at an IR AOI of 40–45° as shown in Figure 2). Figure 7a and b shows the simulated data for two IR AOI (45° and 60°) illustrating the effect described. The simulated data have been normalized to one at the free OH position to simplify the comparison of the relative intensities across the spectral range shown. Figure 7a (IR AOI 45°) predicts that the intensity of the  $r^+$  mode relative to the free OH mode should almost double when the visible AOI is changed from 62° to 74°. However, the experimental results show instead limited or no enhancement as a function of the visible angle of incidence (Figure 8). It is worth noting that the

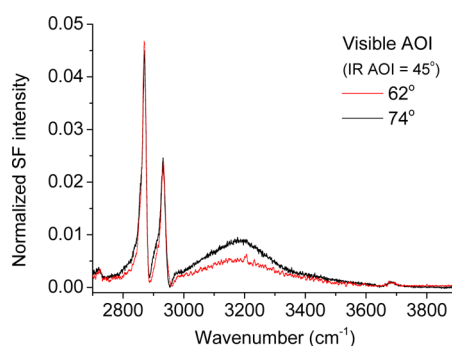


**Figure 8.** Experimental data showing, if anything, a negligible enhancement of the  $r^+$  mode relative to free OH vibration for two selected visible angles of incidence (62° and 74°) at a constant IR angle (45°). A small relative enhancement is seen, however, on the bonded OH band. Data were recorded in the SSP polarization combination and normalized to the Fermi resonance ( $r^+_{FR}$ ) at 2935  $\text{cm}^{-1}$ .

theoretical simulations tend to underestimate the relative intensity of the free OH band at different IR angles of incidence (constant visible AOI), while it is overestimated in the converse case.

#### 4.4. Enhancement in Other Polarization Combinations.

**SPS Polarization.** The theoretical simulations for the variation of the sum frequency intensity in the SPS polarization combination as a function of the angles of incidence (eq 8) are largely similar to those shown for SSP (see Figure S5 in the Supporting Information for an example of a simulated contour plot for the SPS polarization combination). Likewise, in terms of overall enhancement, the recorded spectra generally follow the predicted trends. This is exemplified in Figure 9a where SPS spectra are shown for different visible angles of incidence at a fixed IR AOI of 55°. The overall spectral intensity peaks at approximately 70° as expected from theory. Regarding assignments, note that the strongest band in the spectra is the antisymmetric  $\text{CH}_3$  stretch ( $r^-$ ), and that the free OH band can be easily discerned at 3680  $\text{cm}^{-1}$ . The broad band in the OH stretching region centered at  $\sim 3500 \text{ cm}^{-1}$  is in turn assigned to the asymmetric stretching of hydrogen-bonded water molecules.<sup>44</sup> Moreover, the relative enhancement across the CH and OH stretching regions is also dependent on the IR angle of incidence chosen. As shown in Figure 9b, the free OH signal is preferentially enhanced at an IR AOI of 55° and 60° relative to 45°. Nonetheless, as for the SSP polarization case, this relative enhancement is in quantitative terms higher than what is predicted from theory.

**PPP Polarization.** The SF intensity in the PPP polarization combination is an admixture of four different  $\chi^{(2)}$  elements (eq 9), and consequently four independent combinations of  $L'$ -factors must be considered. Because of their different angular dependence, a judicious choice of angles can be used to preferentially enhance one specific  $\chi^{(2)}$  element, while the others are reduced several orders of magnitude or even completely suppressed.<sup>8,28</sup>

The simulations of the angular dependence for each prefactor of the four  $\chi^{(2)}$  elements contributing to the PPP signal are shown in Figure 10. Note that at the critical angle, the  $L_{xx}$  Fresnel factors are zero for the visible and SF beams, because the P polarized electric field oscillates purely in the  $z$  direction. This is however not the case for the IR-field, due to the imaginary component of the refractive index of water (vide supra). Determining the individual  $\chi^{(2)}$  elements is important for calculating the orientation of specific functional groups at the surface. It can be inferred from the simulations in Figure 10 that the different  $\chi^{(2)}$  elements can be selectively enhanced by recording data at specific angles of incidence. For instance, to

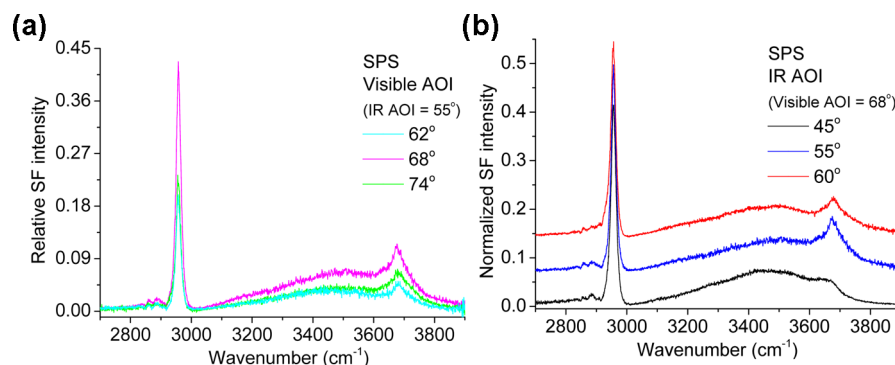


**Figure 9.** (a) Experimental data from the OTS monolayer recorded in the SPS polarization combination at different visible angles of incidence and at a constant IR AOI of 55° (the absolute values of the SF intensity can be directly compared to those in Figure 3a). (b) Experimental SPS spectra for different IR AOI at a constant visible AOI. Note the relative enhancement of the free OH region at 55° and 60° as compared to 45° (spectra have been offset 0.07 units for clarity).



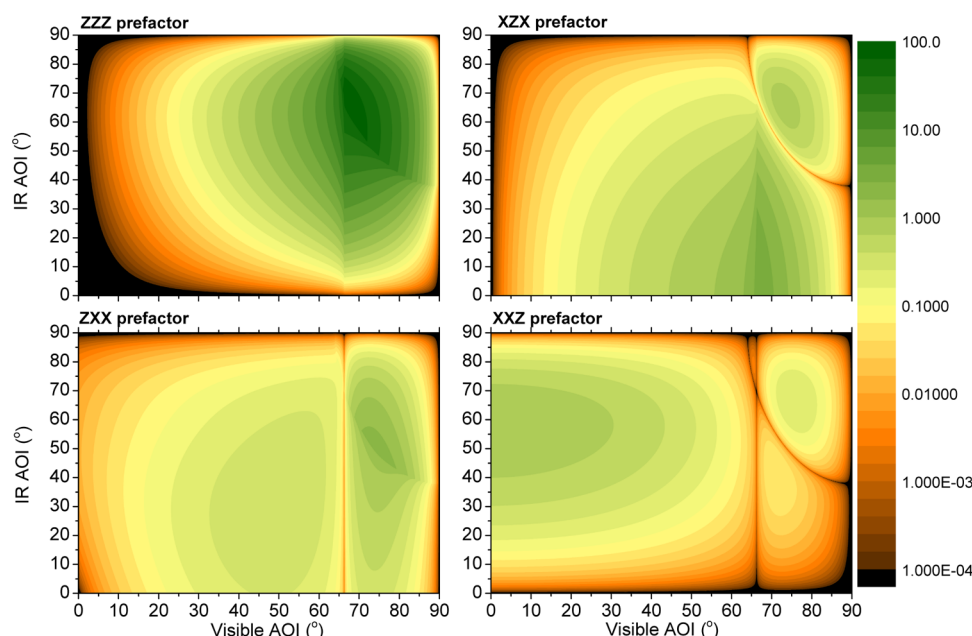


**Figure 10.** Simulation of the contributions to the SF intensity from the various terms involved in the PPP signal as a function of the IR and visible angles of incidence at a fixed IR wavenumber ( $3350\text{ cm}^{-1}$ ). Note the zero intensity at the critical angle for the prefactors involving an  $x$  visible or SF component. The intensity does not go to zero at the critical IR angle due to absorption. The four plots share a common color band scale, normalized to the highest intensity observed in the  $zzz$  plot close to the SF and visible critical angles. The relative intensities between the different prefactors are strongly dependent on the value of  $n'$  chosen, which was here set to 1.2.

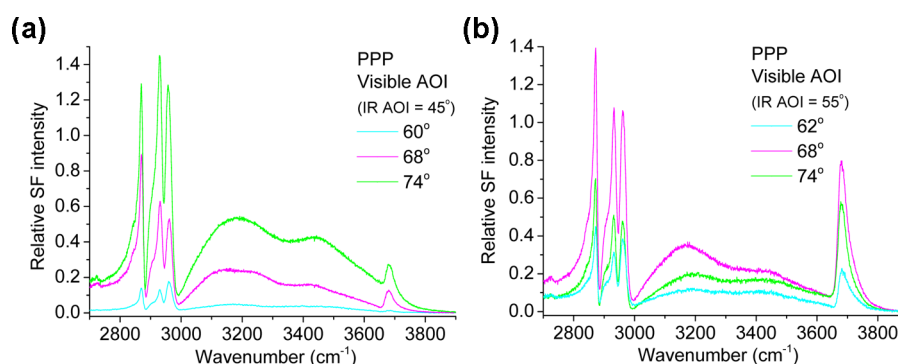


**Figure 11.** Sum frequency spectra of the OTS monolayer collected in the PPP polarization combination for different visible AOI and two IR angles ( $45^\circ$  in (a) and  $55^\circ$  in (b)). According to the simulations, the maximum overall enhancement occurs at a visible AOI of  $74^\circ$ , and at  $\sim 68^\circ$  for spectra shown in (a) and (b), respectively. The free OH region is preferentially enhanced at IR AOI of  $55^\circ$ . The absolute intensities for (b) can be directly compared to those shown in Figures 3a and 9a.

selectively probe the  $zzz$  component, the visible angle can be set to its  $\Theta_c$  to completely suppress the  $zxx$  and  $xxz$  components, while the IR angle is chosen so that the SF beam is emitted at its  $\Theta_c$  (removing the  $xzx$  contribution). In contrast, to selectively enhance the  $xzx$  component, the visible beam is maintained at its  $\Theta_c$  and the IR angle is set to the lowest possible value to reduce the relative contribution of the  $zzz$  prefactor. In a similar manner, the  $xxz$  component is enhanced relative to the other elements at IR angles of incidence around  $60^\circ$  and very low visible angles. Because  $\chi_{zzx}^{(2)}$  equals  $\chi_{zxz}^{(2)}$  it is sufficient to determine one of the two components. Furthermore, the  $\chi_{xxz}^{(2)}$  and  $\chi_{xzx}^{(2)}$  can easily be determined from the SSP and SPS polarization combination, respectively, because for surfaces with  $C_\infty$  symmetry,  $\chi_{xxz}^{(2)} = \chi_{yyz}^{(2)}$  and  $\chi_{zzx}^{(2)} = \chi_{zyz}^{(2)}$ .

Spectra collected under the PPP polarization for the OTS monolayer are shown in Figure 11. Note that at the angles used, the  $\chi_{zzz}^{(2)}$  is preferentially enhanced, because the corresponding

prefactor is from 2 to 6 orders of magnitude stronger than those expected for the other  $\chi^{(2)}$  elements. The spectra in Figure 11 display trends similar to those discussed above. First, the overall spectral intensity increases with larger visible AOI, peaking at the predicted angles. Second, the free OH band is preferentially enhanced relative to the CH stretching modes at IR AOI of  $55^\circ$  and  $60^\circ$  when compared to  $45^\circ$  and almost all other possible angles. Yet again, this relative enhancement does not quantitatively agree with that expected from simulations, which predict a behavior very similar to the one shown in Figure 6b for the SSP polarization combination. Finally, note how the relative intensities between the different modes in the CH stretching region may change with varying angle of incidence as shown in the PPP spectra of Figure 11. This is mainly a consequence of varying contributions of the Fresnel prefactors with the angle of incidence and has to be carefully considered when interpreting spectral features in the PPP spectra.

## 5. SUMMARY AND CONCLUDING REMARKS

The angle of incidence of the visible and IR beams has an important effect on the overall intensity of the SF signal. This enhancement is particularly relevant at interfaces where one or both beams can be delivered close to, or at, total internal reflection conditions. Neglecting practical details, such conditions can in principle be reached at any interface (i.e., solid/liquid, liquid/vapor, liquid/liquid, and solid/vapor interfaces). At the fused silica/water interface studied here, the SF intensity can be increased by several orders of magnitude when selecting incident angles that allow not only the IR and visible beams, but also the emitted SF beam, to be close to the critical conditions. This carries important consequences in the experimental design because choosing the wrong geometry may simply render otherwise routine experiments unfeasible.

The overall enhancement of the SF intensity predicted by the theoretical models has been verified experimentally for a selected number of incident angles and for three different polarization combinations (SSP, SPS, and PPP). In particular, the spectra confirm a strong angular dependence of the SF intensity close to the critical conditions. This stresses the significance of being able to set the angles of incidence in a reproducible manner and with high precision. The spectrometer used for collecting the spectra shown here was designed and built with a high degree of automation, which allows changing the angles of incidence with a precision better than  $0.02^\circ$  in a time frame that ranges from seconds to just a few minutes. Nonetheless, as the laser beams are converging at the surface, in practice they are not delivered at a single angle but rather in a cone of angles, with the spread depending on how tightly the beams are focused (for the IR and visible beams used here, the angular spread was  $\pm 0.9^\circ$  and  $\pm 0.3^\circ$ , respectively). This is highly relevant when considering the effects of the angle of incidence in the SF intensity enhancement, particularly when close to TIR conditions (note that the spread of angles in the IR beam is typically  $\pm 5^\circ$  in most femtosecond SF spectrometers).

Moreover, the spectra recorded at different IR angles of incidence show that the relative enhancement of the spectral features across the CH and OH stretching regions is not equal. Theoretical simulations qualitatively agree with this observation. For instance, to preferentially probe the free OH region, it is more appropriate to use an IR angle of incidence close to  $55^\circ$ , while for the CH stretching region it is better to use an IR angle comprised between  $75^\circ$  and  $80^\circ$ . The uneven enhancement is a consequence of the large dispersion in the refractive index of water across the IR spectral region. Nevertheless, the quantitative agreement between experiments and theory is poor. This is patent in the free OH stretching region, where simulations underestimate by 2–4 times the enhancement observed in the spectra collected at IR angles of  $55^\circ$  (and  $60^\circ$ ) relative to  $45^\circ$  (see Figures 5, 6, and 11). In the same line of thought, the simulations also predict similar changes in the relative enhancement, albeit to a lower extent, when recording spectra at different visible AOI at a constant IR angle. In this latter case, the simulations appear to overestimate the dependence, because the collected spectra show practically no changes with the visible AOI (Figures 7 and 8). The causes of this quantitative disagreement between theory and experiments are not fully understood. However, it appears unlikely they are a consequence of experimental errors or incorrect input

parameters in the theoretical model (i.e., refractive indexes of silica and water). One remaining explanation is that the theoretical model is incomplete. We note that, to the best of our knowledge, the theoretical angular dependence of the SF intensity across this relatively large frequency range (CH and OH stretching regions) has not been systematically verified before.

Although the analysis made here was in principle limited to the silica/water interfaces, the general conclusions, including theoretical graphs, can be directly extrapolated to  $\text{CaF}_2$ /water interfaces, because the refractive indexes of the two solid substrates differ by less than 2%. This is, however, not the case for the sapphire/water interface. The significantly higher refractive index of sapphire results in a translation of the most favorable conditions to lower angles of incidence (AOI close to  $50^\circ$ ) as shown in the Supporting Information (Figure S6).

Varying the angles of incidence can help separating the individual  $\chi^{(2)}$  element's contribution to the SF spectra collected in the PPP polarization combination. This may prove highly useful for determining the orientation of specific functional groups at the surface. Finally, setting the angle of incidence to preferentially enhance one specific spectral region may have practical advantages as will be exploited in a forthcoming publication, when discussing the molecular interpretation of contact angle measurements.

## ■ ASSOCIATED CONTENT

### § Supporting Information

Differences in the Fresnel formulations commonly used in the SF literature; tabulated refractive indexes of water and fused silica across the CH and OH stretching frequencies; spectra showing the resolving power of the SF spectrometer; details of the procedure used to assemble and normalize the raw spectral data; contour plots of SF intensity simulations as a function of IR and visible AOI at selected wavenumbers for the SSP and SPS polarization combination; and simulations of the expected variation of the SF intensity for the sapphire/water interface as a function of the IR and visible AOI. This material is available free of charge via the Internet at <http://pubs.acs.org>.

## ■ AUTHOR INFORMATION

### Corresponding Author

\*Tel.: +46 8 7909915. E-mail: [tyrode@kth.se](mailto:tyrode@kth.se).

### Notes

The authors declare no competing financial interest.

## ■ ACKNOWLEDGMENTS

Funding by the Swedish Research Council (VR) is gratefully acknowledged. E.T. acknowledges financial support from the European Community's Marie Curie Reintegration grant, Molecular Structure in Thin Wetting Films, contract FP7-PEOPLE-ERG-2008 no. 239459. We thank Takuma Nishida and Shen Ye (Hokkaido University, Japan) for inspiring part of this work, as well as Peter Coyne and Malcom Richardson (Durham University, UK) for manufacturing the glass cells used in these studies.

## ■ REFERENCES

- (1) Guyot-Sionnest, P.; Hunt, J. H.; Shen, Y. R. *Phys. Rev. Lett.* **1987**, *59*, 1597–1600.
- (2) Richmond, G. L. *Chem. Rev.* **2002**, *102*, 2693–2724.
- (3) Shen, Y. R.; Ostroverkhov, V. *Chem. Rev.* **2006**, *106*, 1140–1154.

- (4) Bain, C. D. *J. Chem. Soc., Faraday Trans.* **1995**, 91, 1281–1296.
- (5) Chen, Z.; Shen, Y. R.; Somorjai, G. A. *Annu. Rev. Phys. Chem.* **2002**, 53, 437–465.
- (6) Williams, C. T.; Yang, Y.; Bain, C. D. *Langmuir* **2000**, 16, 2343–2350.
- (7) Born, M.; Wolf, E. *Principles of Optics*, 7th ed.; University Press: Cambridge, 1999.
- (8) Löbau, J.; Wolfrum, K. *J. Opt. Soc. Am. B* **1997**, 14, 2505–2512.
- (9) Conboy, J. C.; Messmer, M. C.; Richmond, G. L. *J. Phys. Chem.* **1996**, 100, 7617–7622.
- (10) Knock, M. M.; Bell, G. R.; Hill, E. K.; Turner, H. J.; Bain, C. D. *J. Phys. Chem. B* **2003**, 107, 10801–10814.
- (11) Hsu, P. Y.; Dhinojwala, A. *Langmuir* **2012**, 28, 2567–2573.
- (12) Hatch, S. R.; Polizzotti, R. S.; Dougal, S.; Rabinowitz, P. *Chem. Phys. Lett.* **1992**, 196, 97–102.
- (13) York, R. L.; Li, Y.; Holinga, G. J.; Somorjai, G. A. *J. Phys. Chem. A* **2009**, 113, 2768–2774.
- (14) Gautam, K. S.; Schwab, A. D.; Dhinojwala, A.; Zhang, D.; Dougal, S. M.; Yeganeh, M. S. *Phys. Rev. Lett.* **2000**, 85, 3854–3857.
- (15) Wang, J.; Chen, X.; Clarke, M. L.; Chen, Z. *Proc. Natl. Acad. Sci. U.S.A.* **2005**, 102, 4978–4983.
- (16) Heinz, T. F. Second-order nonlinear optical effects at surfaces and interfaces. In *Nonlinear Surface Electromagnetic Phenomena*; Ponath, H. E., Stegeman, G. L., Eds.; North Holland: Amsterdam, 1991; pp 353–416.
- (17) Shen, Y. R. *Annu. Rev. Phys. Chem.* **1989**, 40, 327–350.
- (18) Wei, X.; Hong, S.-C.; Zhuang, X.; Goto, T.; Shen, Y. R. *Phys. Rev. E: Stat. Phys., Plasmas, Fluids, Relat. Interdiscip. Top.* **2000**, 62, 5160–5172.
- (19) Jena, K. C.; Hung, K.-K.; Schwantje, T. R.; Hore, D. K. *J. Chem. Phys.* **2011**, 135, 044704.
- (20) Hopkins, A. J.; McFearn, C. L.; Richmond, G. L. *J. Phys. Chem. C* **2011**, 115, 11192–11203.
- (21) Tian, C. S.; Shen, Y. R. *Proc. Natl. Acad. Sci. U.S.A.* **2009**, 106, 15148–15153.
- (22) Ye, S.; Nihonyanagi, S.; Uosaki, K. *Phys. Chem. Chem. Phys.* **2001**, 3, 3463–3469.
- (23) Du, Q.; Freysz, E.; Shen, Y. R. *Science* **1994**, 264, 826–828.
- (24) Tong, Y.; Tyrode, E.; Osawa, M.; Yoshida, N.; Watanabe, T.; Nakajima, A.; Ye, S. *Langmuir* **2011**, 27, 5420–5426.
- (25) Vaughan, J. Pulse Shaping. In *Ultrafast Optics Textbook*; Trebino, R., Squier, J., Eds.; GA, 2012; p 25. <http://frog.gatech.edu/>.
- (26) Velarde, L.; Zhang, X.-y.; Lu, Z.; Joly, A. G.; Wang, Z.; Wang, H.-f. *J. Chem. Phys.* **2011**, 135, 241102.
- (27) Colthup, N.; Daly, L. H.; Wiberley, S. E. *Introduction to Infrared and Raman Spectroscopy*, 3rd ed.; Academic Press: San Diego, CA, 1990.
- (28) Bain, C. D. Non-linear optical techniques. *Surfactant Science Series*; Dekker: New York, 1999; Vol. 83, pp 335–373.
- (29) Wang, H.-F.; Gan, W.; Lu, R.; Rao, Y.; Wu, B.-H. *Int. Rev. Phys. Chem.* **2005**, 24, 191–256.
- (30) Lambert, A. G.; Davies, P. B.; Neivandt, D. J. *Appl. Spectrosc. Rev.* **2005**, 40, 103–145.
- (31) Zheng, D.-S.; Wang, Y.; Liu, A.-A.; Wang, H.-F. *Int. Rev. Phys. Chem.* **2008**, 27, 629–664.
- (32) Zhuang, X.; Miranda, P. B.; Kim, D.; Shen, Y. R. *Phys. Rev. B: Condens. Matter* **1999**, 59, 12632–12640.
- (33) Butcher, P. N.; Cotter, D. *The Elements of Nonlinear Optics*; Cambridge University Press: Cambridge, 1990.
- (34) Hirose, C.; Akamatsu, N.; Domen, K. *Appl. Spectrosc.* **1992**, 46, 1051–1072.
- (35) Beattie, D. A.; Fraenkel, R.; Winget, S. A.; Petersen, A.; Bain, C. D. *J. Phys. Chem. B* **2006**, 110, 2278–2292.
- (36) Hale, G. M.; Querry, M. R. *Appl. Opt.* **1973**, 12, 555–563.
- (37) Segelstein, D. J. The complex refractive index of water. Master Thesis, University of Missouri, MO, 1981.
- (38) Malitson, I. H. *J. Opt. Soc. Am.* **1965**, 55, 1205–1208.
- (39) Tyrode, E.; Hedberg, J. J. *J. Phys. Chem. C* **2012**, 116, 1080–1091.
- (40) Scatena, L. F.; Brown, M. G.; Richmond, G. L. *Science* **2001**, 292, 908–912.
- (41) Ordal, M. A.; Long, L. L.; Bell, R. J.; Bell, S. E.; Bell, R. R.; Alexander, J. R. W.; Ward, C. A. *Appl. Opt.* **1983**, 22, 1099–1120.
- (42) Schulz, L. G. *J. Opt. Soc. Am.* **1954**, 44, 357–362.
- (43) Schulz, L. G.; Tangherlini, F. R. *J. Opt. Soc. Am.* **1954**, 44, 362–368.
- (44) Tyrode, E.; Johnson, C. M.; Kumpulainen, A.; Rutland, M. W.; Claesson, P. M. *J. Am. Chem. Soc.* **2005**, 127, 16848–16859.